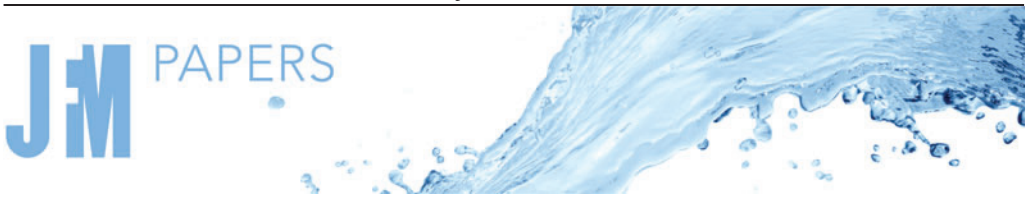
J. Fluid Mech. (2022), *vol*. 946, A21, doi:10.1017/jfm.2022.439



Air entrapment of a neutral drop impacting onto a flat solid surface in electric fields

Yu Tian[1], Yanchu Liu[2], Zihan Peng[1], Chenghao Xu[2], Dong Ye[1], Yin Guan[3], Xinping Zhou[1,4], Weiwei Deng[2,†] and YongAn Huang[1,†]

[1]State Key Laboratory of Digital Manufacturing Equipment and Technology, Huazhong University of Science and Technology, Wuhan 430074, China

[2]Department of Mechanics and Aerospace Engineering, Southern University of Science and Technology, Shenzhen 518055, China

[3]School of Energy and Power Engineering, Huazhong University of Science and Technology, Wuhan 430074, China

[4]School of Mechanical Science and Engineering, Huazhong University of Science and Technology, Wuhan 430074, China

(Received 30 December 2021; revised 28 April 2022; accepted 14 May 2022)

When a charge neutral drop impacts on a flat solid substrate, a small air bubble is always trapped underneath due to the lubrication pressure coming from the viscous stress in the squeezed air film. Herein we find experimentally and numerically that the process of the air entrapment and the initial contact state of the drop with the substrate can be profoundly altered via an external electric field. In an electric field, the induced electric stresses at the bottom of the drop increase drastically right before the drop contacts the substrate, which acts against the lubrication pressure, resulting in reduced initial contact radius and air bubble size. When the external electric field reaches a critical value, the electrical stress accelerates the flow near the bottom of the drop and generates a conical tip quickly instead of a dimple, resulting in a centre contact and eliminating the air bubble entrapment. Based on the dipole mirror charge model, we find the dimensionless strength of critical electric field scales with the square root of capillary number based on the air viscosity. This scaling law of the critical electric field for eliminating the air bubble entrapment is verified experimentally and numerically. This work may offer a new way to mitigate defects caused by air bubble entrapment for inkjet printing and droplet-based additive manufacturing.

Key words: drops, bubble dynamics, electrohydrodynamic effects

† Email addresses for correspondence: yahuang@hust.edu.cn, dengww@sustech.edu.cn

© The Author(s), 2022. Published by Cambridge University Press

https://doi.org/10.1017/jfm.2022.439 Published online by Cambridge University Press

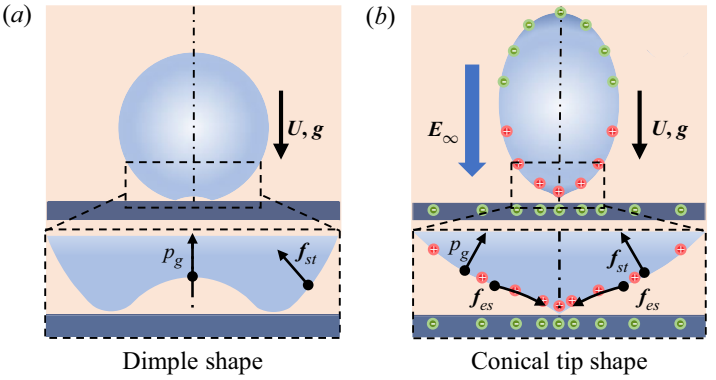


Figure 1. Schematic of the drop before it impacts on the substrate. (*a*) The conventional bottom dimple shape of the drop without the electric field. (*b*) Conical tip shape at the bottom of the drop in the electric field.

1. Introduction

The dynamics of the drop impacting on a solid or pool surface are fundamental subjects of extensive studies (Yarin 2006; Thoroddsen, Etoh & Takehara 2008; Thoraval *et al.* 2013; Josserand & Thoroddsen 2016). An air bubble is often trapped underneath upon drop impact (van Dam & Clerc 2004; Bouwhuis *et al.* 2012; Li, Vakarelski & Thoroddsen 2015; Langley, Castrejon-Pita & Thoroddsen 2020). The air bubble entrapment occurs in a wide range of drop diameters from hundreds of nanometres to millimetres (Thoroddsen, Etoh & Takehara 2003; Shen *et al.* 2016; Yi *et al.* 2016). Hicks & Purvis (2010) found that the air at the bottom of the drop evolves into a film of 1–5 μm thickness before the drop contacts the substrate. When the lubricating pressure of the air (p_g) is strong enough, the bottom of the drop can be deformed into a dimple (Mandre, Mani & Brenner 2009), as shown in figure 1(*a*). The air is trapped by the circular contact line and eventually forms a bubble, which occurs within a hundred microseconds after initial contact. The air bubble entrapment process has been visualized through ultrafast x-ray phase-contrast imaging (Lee *et al.* 2012) or high-speed interferometry technology (Li & Thoroddsen 2015; van der Veen *et al.* 2012). Numerically, Mehdi-Nejad, Mostaghimi & Chandra (2003) used the volume of fluid (VOF) method to track the drop interface and successfully simulated the air bubble entrainment process of water and n-heptane drops impacting on a steel surface and a thin liquid film, respectively. Xiong & Cheng (2018) and Shukla *et al.* (2019) each proposed a new model to simulate the air bubble entrainment process in the molten drop after its impact on the cold smooth surface. Therefore, numerical simulation provides a useful approach for studying the air entrapment and bubble formation processes (Li *et al.* 2017*a*; Jian *et al.* 2020; Kumar *et al.* 2020).

Generally, air bubble entrapment is undesirable in many drop deposition applications (Huang *et al.* 2019; Oratis *et al.* 2020), such as inkjet printing (Minemawari *et al.* 2011) and droplet-based additive manufacturing (Stringer *et al.* 2016; Wu *et al.* 2020). The voids in the printed device become defects and harm the structural integrity and quality of the functional material (Derby 2010; Ligon *et al.* 2017). Li *et al.* (2017*b*) proposed that the size of the bubbles can be shrunk by reducing the ambient pressure, and the double contact phenomenon can be observed when the compressibility parameter exceeds ∼25. However, creating vacuum is not always feasible in many cases. The microstructure has been introduced on the substrate surface to form channels for gas to escape and avoid air bubble entrapment (Antonini *et al.* 2014; Liu, Tan & Xu 2015). In addition, Hicks &

https://doi.org/10.1017/jfm.2022.439 Published online by Cambridge University Press

Purvis (2010) mentioned that no bubbles will be trapped when drops impact with an oblique surface (García-Geijo, Riboux & Gordillo 2020) or a horizontally moving surface. These methods focused on reducing the lubrication pressure of the air to avoid trapping bubbles, while some other ways were proposed to adjust the interface profile at the bottom of the drop. Vo & Tran (2021) performed an interdigital electrode substrate which can deform the drop by the electrophoretic effect, inducing controlled rupture of the air film and creating a channel for air to escape, while it is not convenient enough to modify the electrode on the substrate. Gao *et al.* (2019) proposed a way to charge the drop to a critical charge level so that the bottom of the drop exhibits a microtip deformation, which results in puncturing the air disc to achieve point contact, thus avoiding the air entrapment. A similar double contact state can also be observed in some cases. However, in most practical applications (Singh *et al.* 2010), the drops are electroneutral, and the substrate is horizontal static, flat and smooth. Therefore, it is quite desirable to propose a convenient approach to eliminate the air bubble entrapment without altering the microstructure of the substrate surface or the properties of the drop.

A non-invasive and easy-to-control way to induce drop deformation can be achieved by applying an external electric field (Yang *et al.* 2014; Vlahovska 2019; Wang *et al.* 2021). The external electric field polarizes the drop interface due to the difference in dielectric constant and conductivity on both media, and electrical stress will be generated at the interface (Zhang, Zahn & Lin 2013; Sengupta, Walker & Khair 2017). The drop will stretch and deform along the direction of the electric field, and even become atomized (Collins *et al.* 2013), depending on the strength of the electric field and the fluid characteristics (density, viscosity, permittivity and conductivity) (Gawande, Mayya & Thaokar 2020; Taylor 1966; Wagoner *et al.* 2020). Such electrohydrodynamic (EHD) deformation of the suspended drop under electric fields has been extensively studied (Santra, Mandal & Chakraborty 2018). However, there is little research reported on the dynamic process of drop impact on the flat solid substrate in an electric field, and even less on the EHD behaviour of air entrapment, which is a fresh EHD subject. The drops are subjected to deformation by electrical stress in an electric field, which may fundamentally change the impact dynamics, air film formation and the bubble entrapped behaviour.

In this study, we numerically and experimentally investigated the EHD behaviour of the air entrapment in a charge neutral drop impact in an external electric field. We show that as the drop approaches the substrate with a separation of <1 mm, the polarized surface charges at the bottom of the drop, causing the bottom electrical stresses to increase rapidly with the inverse square of the distance δ between the drop and substrate. The electric stress cancels part of the retarding effect of the lubrication pressure, resulting in a changed drop surface shape before the contact with the substrate, thereby regulating the evolution of the subsequent air film entrapment and the initial contact radius, as shown in figure 1(*b*). The internal flow and the electric force field at the bottom of the drop during the air entrapment altered by the electric field are revealed through simulations. A scaling law of the critical external electric field for eliminating air entrapment is derived based on a dipole charge mirror model.

The paper is organized as follows. The experimental set-up and numerical model are presented in § 2. In § 3, we discuss the difference of the drop impact and air entrapment in external electric fields and explain the effect mechanisms of the electric field. In § 4, we give a theoretical expression of a critical external electric field, in which no bubble is trapped by analysing the competition of the forces on the drop. In § 5, we provide the conclusions of our work.

https://doi.org/10.1017/jfm.2022.439 Published online by Cambridge University Press

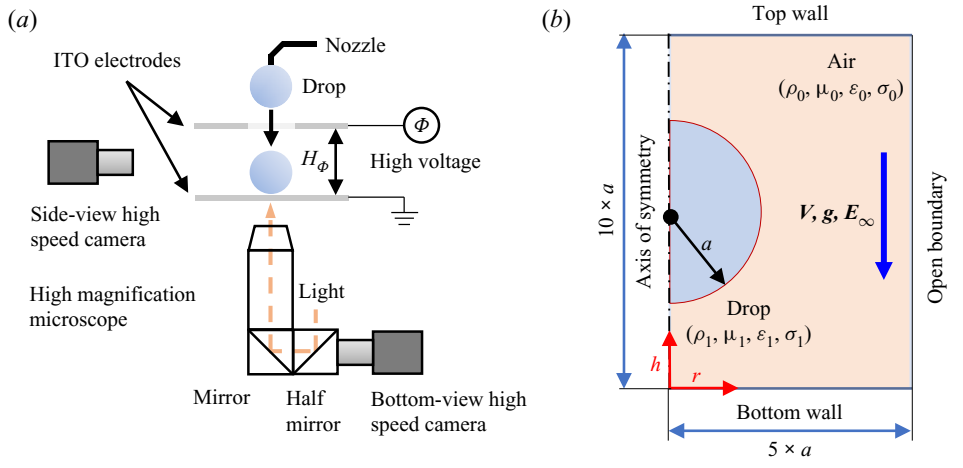


Figure 2. (*a*) Schematic of the experimental set-up. (*b*) Schematic of a leaky dielectric drop impacts in an electric field.

2. Experimental set-up and numerical model

2.1. *Experimental set-up*

The experimental set-up is shown schematically in figure 2(*a*). The domain of interest is between the top electrode and the grounded substrate. The voltage difference Φ and separation H between the top electrode and substrate define an approximately uniform electric field $\boldsymbol{E}_\infty = \Phi/H_\Phi$. A circular hole is laser drilled in the top electrode, to allow the drop released from a nozzle to enter the electric field. Both the electrode and the substrate are glass slides coated with indium tin oxide (ITO), providing both electrical conductivity for the electric field and optical transparency for bottom-view illumination. The specific size of glass slides is $75 \times 25 \times 0.7$ mm^3 and the thickness of ITO coating is 125 nm. A 500 nm-thick polymethyl methacrylate film is spin coated on the ITO substrate and modified with octadecyltrichlorosilane, which avoids charging the drop and ensures the contact angle of the water is 90°. We use a high-speed video camera (i-SPEED 726, iX Cameras) at frame rates up to 272 251 fps with a high-intensity coaxial white light to capture the fast initial contact. The resolving power is up to 1.35 µm pixels^{-1} and the exposure time is down to 289 ns. The impacting events from the side view are recorded with an i-SPEED 220 camera. Deionized water is used as the liquid and drops are generated by pumping the liquid pneumatically through a stainless steel capillary with an outer diameter of 160 µm, resulting in an equivalent spherical radius of $a = 1.25 \pm 0.01$ mm. Both the capillary and the bottom ITO are grounded to prevent the drops from carrying charges. The release heights between the nozzle and the substrate are 15–200 mm, corresponding to the impact velocities $\boldsymbol{U} = 0.5{-}2$ m s^{-1}. All the experiments are carried out at ambient pressure with room temperature. The experimental parameters are shown in table 1.

2.2. *Numerical model*

The drop impact process in the electric field can be simplified by using a two-dimensional axisymmetric model (figure 2*b*). The size of the computational domain is set to $5a \times 10a$. A numerical model combines the finite volume method and the leaky dielectric model

https://doi.org/10.1017/jfm.2022.439 Published online by Cambridge University Press

Liquid	a (mm)	ρ (kg m^{-3})	μ (Pa s)	σ (S m^{-1})	ε_r	γ (mN m^{-1})	We
Air	—	1.205	1.79×10^{-5}	1×10^{-50}	1.00	72.7	—
Drop	1.25 ± 0.01	998	1×10^{-3}	5.5×10^{-6}	80.18		$8.6 \sim 214.5$

Table 1. Properties of the air and drop used in the experiments and numerical simulations. Here a is the radius of the drop; ρ is the liquid density; μ is the dynamic viscosity; σ is electrical conductivity; ε_r is the relative permittivity; $\varepsilon_0 = 8.85 \times 10^{-12}$ is the dielectric constant of vacuum. The subscripts 0 and 1 represent air and drop, respectively.

(LDM) is used here. The VOF method is adopted to track the interface of the liquid by the volume fraction α in a computational cell with its value in [0, 1], where 0 and 1 represent air and liquid, respectively. The interface of the air and drop is described by a thin layer of discrete basic computational volumes (Herrada *et al.* 2012). The LDM assumes that the charge is only distributed at the liquid interface of the two-phase because the charge relaxation time ($t_E = \varepsilon/\sigma$) is much shorter than the viscous time of fluid motion ($t_\mu = \rho a^2/\mu$) (Saville 1997). The continuity and momentum equations are

$$\nabla \cdot \boldsymbol{U} = 0, \tag{2.1}$$

$$\frac{\partial(\rho \boldsymbol{U})}{\partial t} + \nabla \cdot (\rho \boldsymbol{U}\boldsymbol{U}) = -\nabla p + \nabla \cdot (\mu[\nabla \boldsymbol{U} + \nabla \boldsymbol{U}^{\mathrm{T}}]) + \rho \boldsymbol{g} + \boldsymbol{f}_{st} + \boldsymbol{f}_{es}, \tag{2.2}$$

$$\boldsymbol{f}_{st} = \gamma \kappa \left(\nabla \alpha\right), \kappa = \nabla \cdot \left(\frac{\nabla \alpha}{|\nabla \alpha|}\right), \tag{2.3}$$

where the additional terms $\boldsymbol{f}_{st}$ and $\boldsymbol{f}_{es}$ are the surface tension stress and the electric stress acting at the interface of two phases, respectively. Surface tension stresses $\boldsymbol{f}_{st}$ are obtained according to the continuous-surface-force model, where κ is the local curvature of the interface. The electric field ($\boldsymbol{E}$) is irrotational and we have

$$\nabla \times \boldsymbol{E} = 0, \quad \boldsymbol{E} = -\nabla \Phi. \tag{2.4a,b}$$

The charge density (ρ_e) can be solved by Gauss's theorem:

$$\rho_e = \nabla \cdot (\varepsilon \boldsymbol{E}) = -\nabla \cdot (\varepsilon \nabla \Phi). \tag{2.5}$$

Therefore, the electric stress $\boldsymbol{f}_{es}$ is

$$\boldsymbol{f}_{es} = \rho_e \boldsymbol{E} - \tfrac{1}{2}\boldsymbol{E}^2 \nabla \varepsilon. \tag{2.6}$$

Here the framework of OpenFOAM is chosen to implement the EHD model (Roghair *et al.* 2015). A second-order implicit algorithm is used in the non-stationary term and the QUICK format is used in convection items. The diffusion term adopts the central difference format. An adaptive time step is used here to improve computational efficiency and the minimum time step is 10^{-7} s. To ensure numerical continuity and stability, the Courant number is set to be <0.5, which represents the relative relationship between the time step and the grid size. Convergence of the solution is confirmed by checking the grid independence of the calculation results. For the bottom air film evolution area, the grid is further refined into 0.2 µm (see supplementary figure S1 available at https://doi.org/10.1017/jfm.2022.439). It should be noted that the contact angle changes dynamically with the speed of the free surface advancing or retreating in reality (Snoeijer & Andreotti 2013). To simplify the model and focus on the effect of the electric field, a static contact angle

https://doi.org/10.1017/jfm.2022.439 Published online by Cambridge University Press

of 90° (also consistent with experimental conditions) is selected in this study. There is a slight difference in time between the simulation and the experiment due to the imperfect substrate and the static contact angle model, which does not affect the key deformation behaviour of the drop before contact.

Generally, the impact processes are first characterized by the Weber number and the capillary number, defined with the liquid properties as

$$We = \frac{\rho_1 2aU^2}{\gamma}, \quad Ca_g = \frac{\mu_0 U}{\gamma}, \tag{2.7a,b}$$

where Ca_g is defined based on the air viscosity. The Taylor limit of critical field ($\boldsymbol{E}_T$) is the maximum electric field strength, at which the drop can maintain a stable shape without spraying or fragmentation in an external electric field (Grimm & Beauchamp 2005):

$$\boldsymbol{E}_T = \frac{c}{2(\pi)^{1/2}} \left(\frac{\gamma}{\varepsilon_0 a}\right)^{1/2}. \tag{2.8}$$

For water in the air, Basaran & Scriven (1989) gave the value of c as 1.625 by fitting the experimental parameters. A dimensionless electric field intensity level is defined to quantify the intensity of the electric field ($\boldsymbol{E}_\infty$):

$$\Gamma_E = \boldsymbol{E}_\infty / \boldsymbol{E}_T. \tag{2.9}$$

Hicks *et al.* (2012) gave the theoretical prediction of the initial contact radius (L_0) of the drop deposited on the substrate based on an incompressible model,

$$L_0 = 3.8 \left(\frac{4\mu_0}{\rho_1 U}\right)^{1/3} {a_B}^{2/3}, \tag{2.10}$$

where a_B is the local radius of curvature at the bottom of the drop. The simulation results of L_0 for drop deposition without electric field at different velocities are verified in supplementary figure S2.

3. Experimental and numerical results

3.1. *The drop impact behaviour in an electric field*

The drop impact event is observed from a side view and bottom view synchronously, and the simulation results complement the limitations of experiment (such as features less than the resolving power of the imaging system and unobservable physical field information). We use the bottom view to observe the film interference fringes (i.e. Newton's ring) caused by light transmission and reflection between the drop interface and glass surface, which provides quantitative information of the air film radius.

Figure 3(*a*) shows the typical process of neutral drop impact on the substrate ($\Gamma_E = 0$, $We = 8.6$) from experiment and simulation. A dimple appears at the bottom of the drop right before the drop impacts the substrate. Then the dimple widens and a ring contacts with the substrate, resulting in an air disc being captured, whose radius and thickness are 253.6 μm and 8 μm, respectively ($t = 0$ ms). During the subsequent spreading of the drop, the air disc shrinks into a small bubble at the bottom of the drop. The bottom-view images in experiment and the simulation images in figure 3(*b*) show the evolution of air film after the drop contacts with the substrate. Before the drop contacts the substrate, a small white spot appears caused by the reflection from the drop bottom surface due

https://doi.org/10.1017/jfm.2022.439 Published online by Cambridge University Press

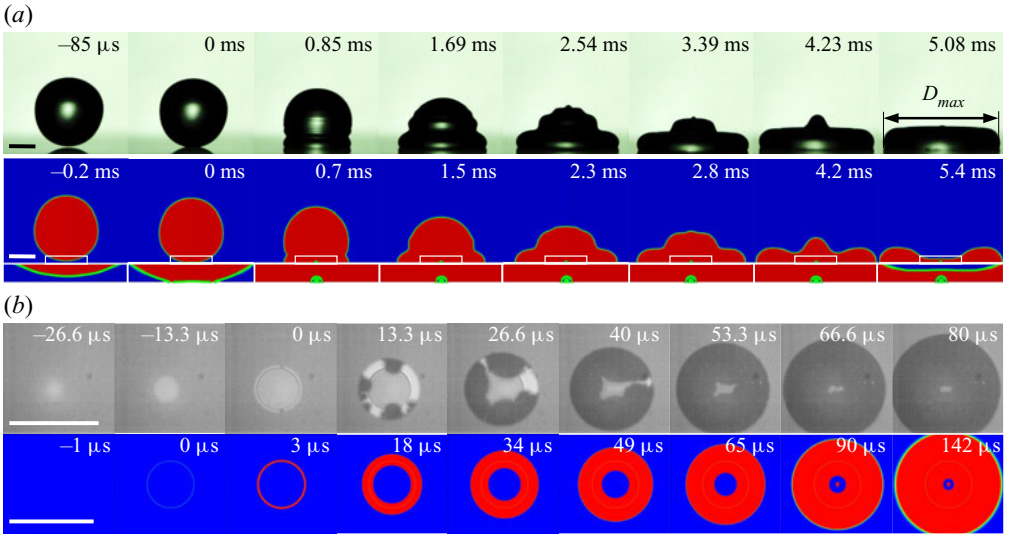


Figure 3. (*a*) Without electric field ($\Gamma_E = 0$), the spreading processes of the normal drop impacting on a smooth dry substrate from experiment and simulation, where a bubble is entrapped underneath. (*b*) The air entrapment is observed from the bottom-view image and the slices images in the simulation. The substrate is wet from the edge air film which subsequently shrinks into a bubble. The drop impacts the substrate at $We = 8.6$ ($Ca_g = 1.23 \times 10^{-4}$). The scale bar is 1 mm. See supplementary movie 1.

to the dimple deformation at the bottom of the drop ($t = -26.6, -13.3\,\mu$s). Next, the substrate is wet inward from the circumference position of the Newton's ring at $t = 0\,\mu$s. However, the substrate surface is not free of contamination or particles, the liquid usually wet from the random points of the circumference. At $t = 66.6\,\mu$s, the wetting region is closed, suggesting the air film is trapped at the bottom of the drop. The trapped bubble is sealed on the substrate inside the drop, similar to typical images reported in the literature (Liu, Tan & Xu 2013).

Figure 4(*a*) shows a very different drop impact process when an electric field of $\Gamma_E = 0.77$ is applied. The drop becomes ellipsoidal with the electric field ($t = -85\,\mu$s). Right before the drop contacts the substrate ($t = 0$ ms), the top half of the drop is still spherical while the bottom half forms a conical tip and makes centre touchdown without trapping any air bubble. This is also observed from the bottom view in figure 4(*b*), where the dark circular disc instead of interference fringes appears. Compared with the phenomenon of drop impact without electric field, it takes more time for the drop to spread to reach the maximum radius when the electric field is present, while the maximum radius is similar in both cases. The experimentally observed phenomena are consistent with simulations.

Figure 5(*a*) shows the spatial electric potential (Φ), the polarization charge density (ρ_e) and the vector of electric stress ($\boldsymbol{f}_{es}$) at the interface as the drop approaches the substrate. The same number of negative and positive charges are distributed on the top and bottom half of the drop surface, respectively. The electrical stress is generated at the interface by the electric field, which deforms the drop. The peak electric field and the maximum electric stresses are all located at both poles of the drop along the vertical direction. The electric stresses deform the drop into an ellipsoid with a vertical long axis. Notably, the charge density (ρ_e) at the bottom of the drop increases drastically right before the drop touches the substrate, resulting in the enhancement of the electric field ($\boldsymbol{E}_B$) and the electric stress ($\boldsymbol{f}_{es}$). Such substantial increase in $\boldsymbol{E}_B$ and $\boldsymbol{f}_{es}$ only occurs within a 1 mm space

https://doi.org/10.1017/jfm.2022.439 Published online by Cambridge University Press

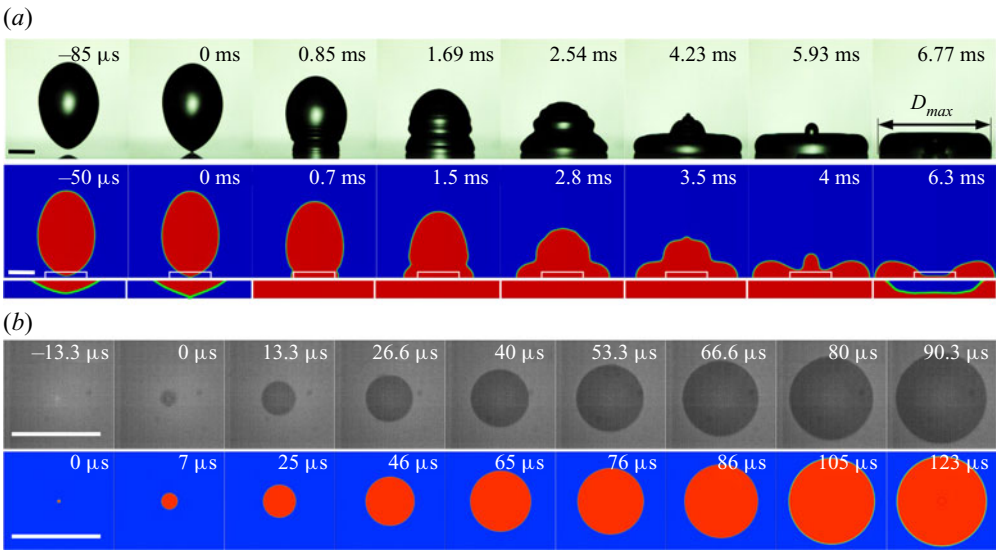


Figure 4. (*a*) With the electric field ($\Gamma_E = 0.77$), the spreading processes of the drop impacting on a smooth dry substrate from experiment and simulation. A Taylor conical is formed at the bottom of the drop, which results in a point contact and eliminates the formation of compressed air film and air bubble entrapment. (*b*) The interference fringe and air disc have both disappeared and are replaced by a growing dark circular disc. It means that the wetting area expands from the central spot to an outward spot, and the air film avoids being entrapped. The drop impacts the substrate at $We = 8.6$ ($Ca_g = 1.23 \times 10^{-4}$). The scale bar is 1 mm. See supplementary movie 2.

between the drop to the substrate ($\delta < 1$ mm). Figure 5(*b*) shows that the ρ_B increases rapidly from 0.1 to 7.2 C m^{-3}, or 72-fold, as δ decreases from 1 mm to 10 μm, while $\boldsymbol{E}_B$ and $\boldsymbol{f}_{esB}$ increase from 3.5×10^5 to 6.5×10^7 V m^{-1} (200-fold) and from 7.4×10^4 to 4×10^{10} N m^{-3} (1×10^6-fold), respectively. The dramatic increase in $\boldsymbol{f}_{esB}$ accelerates the velocity of the drop bottom ($\boldsymbol{U}_B$) from 0.5 m s^{-1} to nearly 10 m s^{-1} before contact. The intense electric stress also causes a conical tip and leads to a point contact of the drop on the substrate without trapping any bubble.

The evolution of the local streamline and pressure field are compared in detail during the contact process. In the absence of electric field ($\Gamma_E = 0$), the left-hand subpanel of figure 6(*a*) shows that the streamline within the drop is downward before contact as the whole drop descends with the same impact velocity. Next, the bottom streamlines are deflected outward due to the deceleration of the drop bottom and increase of the air film pressure. The initial contact radius (L_0) is 253.6 μm when the drop touches the substrate, and the pressure peaks at the initial contact position as shown in the right-hand subpanel of figure 6(*a*). Here the gauge pressure is used. At $t = 115$ μs, the air film recoils into a toroidal bubble, which converges rapidly to the centre and is pinched off at $t = 135$ μs, generating a tiny secondary (daughter) drop on the substrate. The bubble process is consistent with the experimental phenomenon in Thoroddsen *et al.* (2005) and Lee *et al.* (2012).

With the external electric field ($\Gamma_E = 0.77$) in figure 6(*b*), the streamlines begin to converge towards the contact centre when a conical tip is formed. Due to the intense electric stress that pulls the bottom surface to form the conical tip, a zone of negative gauge pressure is formed near the contact centre, and the local pressure gradient gives rise to the flow velocity near the conical tip. After the contact, the substrate is gradually wetted

https://doi.org/10.1017/jfm.2022.439 Published online by Cambridge University Press

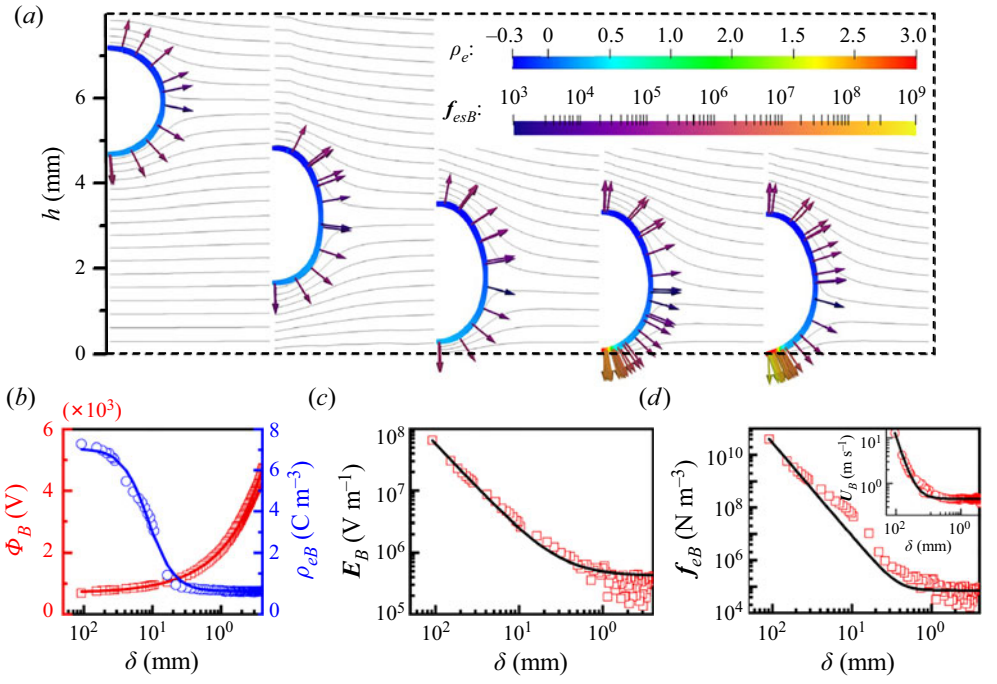


Figure 5. (*a*) Diagram of the spatial electric potential (Φ), polarization charge density (ρ_e) distribution and vector of electric stresses ($\boldsymbol{f}_{es}$) at the interface during the drop falling. (*b*) The potential (Φ_B) and polarization charge density (ρ_{eB}), (*c*) electric field strength ($\boldsymbol{E}_B$), (*d*) electric stresses ($\boldsymbol{f}_{esB}$) and velocity ($\boldsymbol{U}_B$) of the bottom point of the drop vary with the distance δ between the drop and substrate. The drop impacts the substrate at $We = 8.6$ ($Ca_g = 1.23 \times 10^{-4}$) in an electric filed $\Gamma_E = 0.77$. See supplementary movie 3.

from the centre to the periphery and the pressure is higher near the contact line due to the excessive local curvature. It is worth noting that during the spreading process, there is no whirlpool at the centre.

3.2. *The air entrapment varying under different* $\boldsymbol{E}_\infty$

The drop undergoes an ellipsoidal deformation accompanied with weak oscillations caused by electric stresses when falling through the electric field. At the moment of initial contact, the drop deformation aspect ratio D is defined as $D = (l_2 - l_1)/(l_2 + l_1)$ (Ha & Yang 2000), where l_1 and l_2 are the lengths of the vertical and parallel axis of the deformed drop relative to the electric field, respectively (see figure 7). For the same $We = 34.3$, as the external electric field increases, the drop is elongated more seriously with higher aspect ratio D (from 0.03 at $\Gamma_E = 0$ to 0.35 at $\Gamma_E = 0.85$). At the same electric field $\Gamma_E = 0.85$, as the velocity of the drop decreases, the aspect ratio D increases from 0.35 at $We = 34.3$ to 0.43 at $We = 8.6$. The larger deformation occurs with lower We and higher Γ_E, which results in the bottom of the drop becoming sharper and the conical tip being formed more easily. This can be explained as follows. First, there is less time for a faster descending drop to respond to the electric field and deform. Second, a higher pressure of the air film is generated with a larger velocity for the drop, which works against the deformation caused by the electric field.

Figure 8(*a*) shows the initial contact radius L_{0E} shrinks with the increase of Γ_E, and the contact moment is identified by the appearance of dark spots, which are caused by the reduced light reflection after the drop wets the ITO substrate. As Γ_E increases, three

https://doi.org/10.1017/jfm.2022.439 Published online by Cambridge University Press

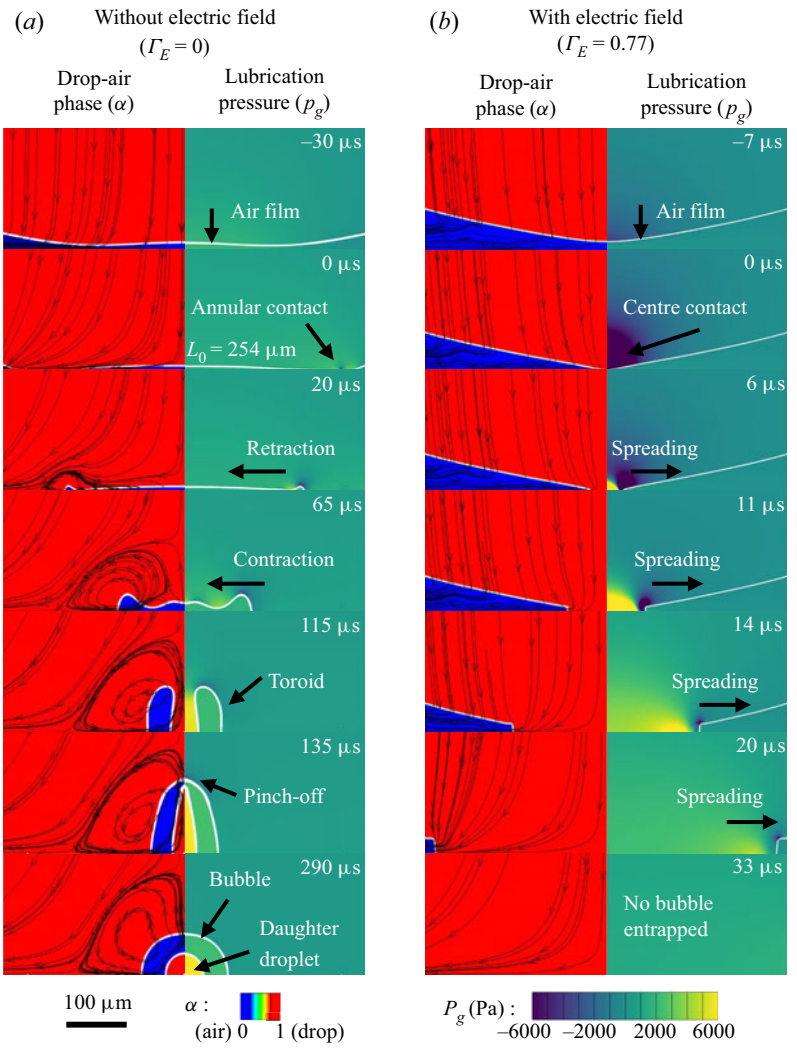


Figure 6. Comparison of evolution sequence diagrams of local streamline and pressure field at the bottom of the drops with and without an electric field. The white curves in the diagrams are the profile of the air film. (*a*) When no external electric field is applied ($\Gamma_E = 0$), due to the deformation of the bottom and the subsequent contraction of the air film, the streamline begins to bend towards the centre. With the evolution of the air film, capillary waves appear, resulting in local vortices in the internal flow field. At the same time, the generation of capillary waves leads to local pressure peaks. Here the gauge pressure is used. (*b*) When an external electric field is applied ($\Gamma_E = 0.77$), the internal flow field of drops always follows the direction from the centre to the periphery, and local pressure peak appears only at the wet edge due to excessive local curvature. The drop impacts the substrate at $We = 8.6$ ($Ca_g = 1.23 \times 10^{-4}$). The scale bar is 100 μm. See supplementary movie 4.

representative distinct contact modes can be observed sequentially from the bottom view, which bears certain similarity to the contact states of charged drop (Gao *et al.* 2019) and under reduced air pressure (Li *et al.* 2017*b*), respectively. (i) Annular contact with reduced air disc radius (annular contact mode): at $\Gamma_E = 0.12$, the initial contact radius $L_{0E} = 41$ μm is only 1/6 of the normal initial radius L_0. The air disc retracts into a small bubble subsequently in figure 8(*b*). (ii) Multiple contact with concentric circular air rings

https://doi.org/10.1017/jfm.2022.439 Published online by Cambridge University Press

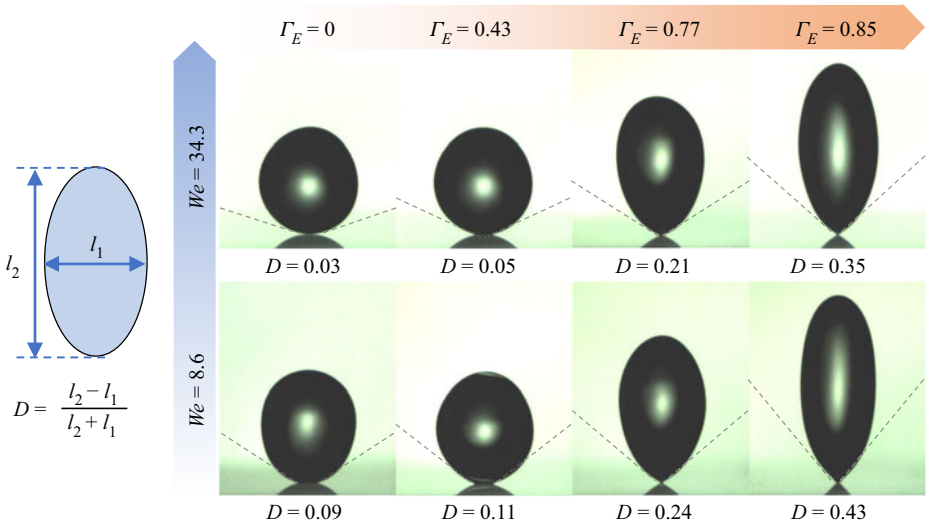


Figure 7. Ellipsoidal drops with different deformation aspect ratios D at the moment of initial contact in various electric fields. As the external electric field increases (Γ_E varies from 0 to 0.85), D becomes higher, from 0.03 to 0.35 ($We = 34.3$)($Ca_g = 2.46 \times 10^{-4}$) and from 0.09 to 0.43 ($We = 8.6$) ($Ca_g = 1.23 \times 10^{-4}$), respectively. See supplementary movie 5.

(multiple contact mode): at $\Gamma_E = 0.14$, the centre contact appears ($L_{0E} = 0\,\mu$m) while there is also a second outer contact trapping a circular air ring, which is pinched off and shrinks into small bubbles. The outer contact occurs multiple times at the wetting edge subsequently, resulting in small bubbles distributed in concentric circles in figure 8(*c*). (iii) Centre contact without any air bubble trapped (centre contact mode): at $\Gamma_E = 0.15$, only the centre contact occurs and the wetting area expands from the central spot to a growing dark circular disc without any air bubble bigger than 1.35 μm being captured in figure 8(*d*). Varying as the external electric field Γ_E in numerical simulation, three representative contact modes can also be obtained in figure 9, which are the same as the experiment. With some precision, there is a relatively quantitative agreement between experiments and simulations using the two-dimensional axisymmetric model, although a completely precise agreement is not achievable due to the three-dimensional effects and the impossibility of accurately modelling solid substrate conditions. For example, the gas film at contact is slightly elliptical (possibly due to the drop oscillations during falling and the substrate is not perfectly horizontal) and the circularly distributed small bubbles formed at the secondary contact. In the following, we explain the EHD mechanism of the three contact modes mentioned above in an external electric field.

The key parameters of the profile of the drop bottom are compared in figure 10. The time interval between data sets is 20 μs. Figure 10(*a–c*) shows that the drop bottom begins to deform by the thin air cushion beneath for $h = 20\,\mu$m at $\Gamma_E = 0.17$. This is because the pressure at the bottom centre is highest, which decelerates the bottom surface of the drop. Then the drop deformation develops into a dimple with the air disc expanding further and the peak pressure location moving to the contact line. Meanwhile, the charge density increases at the edge of the air disc due to the higher curvature, thus producing large electric stresses there. This leads to the increase of the instantaneous velocity of the drop surface at the edge of the air disc. Compared with the drop impact without electric field, the

https://doi.org/10.1017/jfm.2022.439 Published online by Cambridge University Press

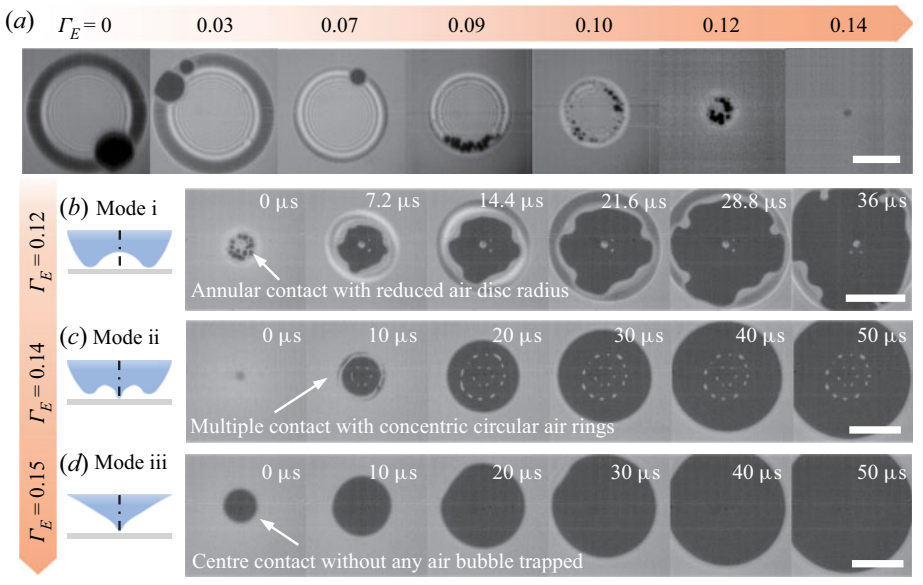


Figure 8. Bottom-view images for representative contact states with different electric field strengths Γ_E. (*a*) The initial contact radius L_{0E} reduced with the increase in Γ_E. (*b*) Annular contact with reduced air disc radius when $\Gamma_E = 0.12$. (*c*) Multiple contact with concentric circular air rings when $\Gamma_E = 0.14$. (*d*) Centre contact without any air bubble trapped when $\Gamma_E = 0.15$. The shape of the drop bottom surface is schematically illustrated on the left-hand side. The drop impacts the substrate at $We = 8.6$ ($Ca_g = 1.23 \times 10^{-4}$). The scale bar is 200 μm. See supplementary movie 6.

earlier touchdown reduces the air disc's further expansion and leads to a smaller contact radius.

When the electric field increases to $\Gamma_E = 0.26$, the bottom of the drop sharpens up before $h = 20\,\mu\text{m}$ (see figure 10*d–f*). The polarized charges accumulate at the lowest surface of the bottom and dramatically increase the electric stresses ($\boldsymbol{f}_{esB}$), which accelerates the drop bottom surface to higher velocity ($\boldsymbol{U}_B$). Meanwhile the bottom of the drop forms a dimple around the centre in figure 10(*d–f*). This is because the wetting area does not expand sufficiently quickly ($\boldsymbol{U}_B = 2.5\,\text{m}\,\text{s}^{-1}$ at $\Gamma_E = 0.26$) and the air around the contact centre is still compressed by the falling drop, and the lubrication pressure peaks at $r = 50\,\mu\text{m}$. Consequently, a secondary contact is formed and an air toroid is entrapped. The evolution of the trapped air film is shown in supplementary figure S4(*b*,*d*).

With the electric field further increased to $\Gamma_E = 0.34$, the radius of the curvature of the drop bottom decreases due to the more concentrated polarized charges and associated enhancement in electric stresses (see figure 10*g–i*). Therefore, the air film at the bottom remains connected to the open space, without trapping any air. In addition, the speed of the expending contact line is relatively high ($\boldsymbol{U}_B = 4\,\text{m}\,\text{s}^{-1}$ at $\Gamma_E = 0.34$) and no subsequent contact occurs, which is defined as a centre contact mode. (Specific data of ρ_e and $\boldsymbol{E}$ of the profile of the drop bottom in the three contact modes mentioned above are provided in the supplementary figure S5.)

Figure 11(*a*) shows the profiles of the drop bottom at the contact moment with $We = 8.6$ with different Γ_E. The initial contact radius (L_{0E}) decreases as Γ_E increases, leading to the change of the contact mode from the annular contact mode to the multiple contact mode or centre contact mode. This is confirmed by the bottom-view images (see supplementary figure S3). Figure 11(*b*) shows the dimensionless initial contact radius ($Z = L_{0E}/L_0$) at

https://doi.org/10.1017/jfm.2022.439 Published online by Cambridge University Press

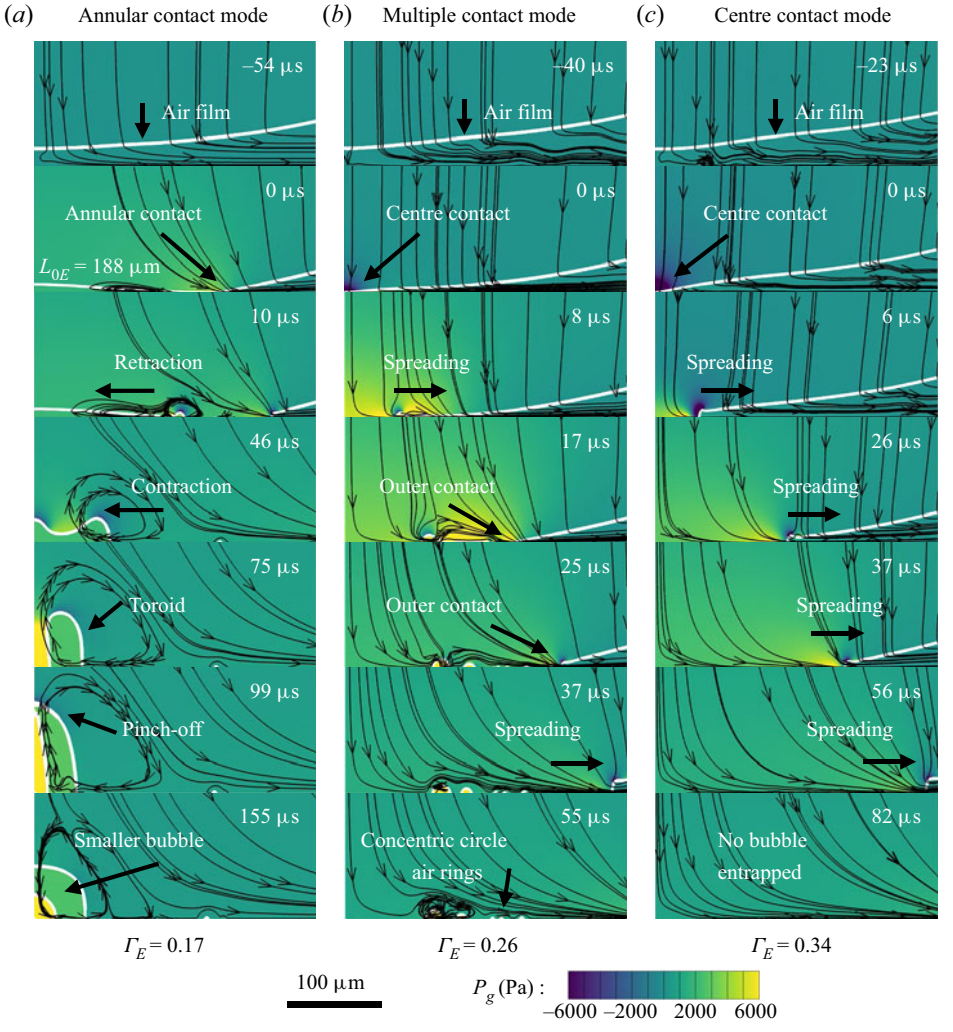


Figure 9. Comparison of evolution sequence diagrams of local streamline and pressure field at the bottom of the drops with different Γ_E in numerical simulations. The white lines in the diagrams are the profile of the air film. (*a*) Annular contact mode when $\Gamma_E = 0.17$. (*b*) Multiple contact mode when $\Gamma_E = 0.26$. (*c*) Centre contact mode when $\Gamma_E = 0.34$. The drop impacts the substrate at $We = 8.6$ ($Ca_g = 1.23 \times 10^{-4}$). See supplementary movie 6.

various Γ_E with different impact velocities. The data can be fitted by $Z = 1 - c_1 \Gamma_E^{c_2}$, where c_1 and c_2 depend on the impact velocity; Z decreases with stronger Γ_E. However, the effect of Γ_E is not as significant for higher We. This confirms the experimental finding that the bottom of the drop is determined by both U and Γ_E.

4. Scaling law of critical electric field

4.1. *Mirror charge model*

The surface charge induced by the electric field affects the electric field in the domain simultaneously, due to the coupling between the charge and the electric field. Taylor (1966) gave an analytical solution to the electric field of a suspended drop in the electric field

https://doi.org/10.1017/jfm.2022.439 Published online by Cambridge University Press

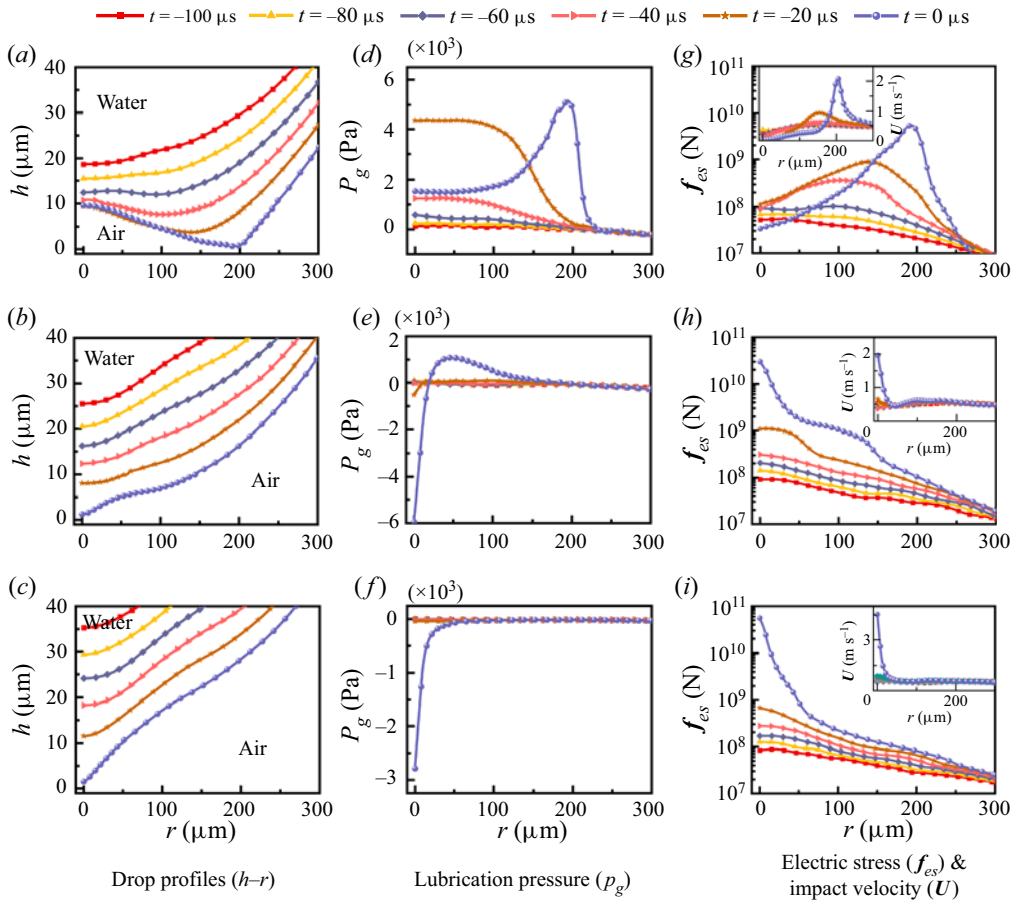


Figure 10. Comparison of the key parameters of the profile of the drop bottom surface in representative contact states before the touchdown. (*a–c*) Annular contact mode at $\Gamma_E = 0.17$. (*d–f*) Multiple contact mode at $\Gamma_E = 0.26$. (*g–i*) Centre contact mode at $\Gamma_E = 0.34$. Panels (*a*,*d*,*g*) show the profiles of the bottom of the drop. Panels (*b*,*e*,*h*) show the lubrication pressure distribution on the profiles. Panels (*c*,*f*,*i*) show the electric field stress distribution on the profiles, whereas the inset shows the velocity distribution on the profiles. Here the drop impacts the substrate at $We = 8.6$ ($Ca_g = 1.23 \times 10^{-4}$). The time interval is 20 μs.

when the drop deformation is small (see figure 12*a*). The spatial potential Φ_0 in polar coordinates (r, θ) is

$$\Phi_0 = \left(r + \frac{1 - R}{2 + R}\frac{a^3}{r^2}\right) \boldsymbol{E}_\infty \cos\theta, \tag{4.1}$$

where $R = \sigma_1/\sigma_0$ is the electrical conductivity ratios. The electric field along the radius direction (r) is

$$\boldsymbol{E}_{0r} = -\frac{\partial \Phi_0}{\partial r} = -\left[1 + \frac{2(R-1)}{2 + R}\frac{a^3}{r^3}\right] \boldsymbol{E}_\infty \cos\theta. \tag{4.2}$$

https://doi.org/10.1017/jfm.2022.439 Published online by Cambridge University Press

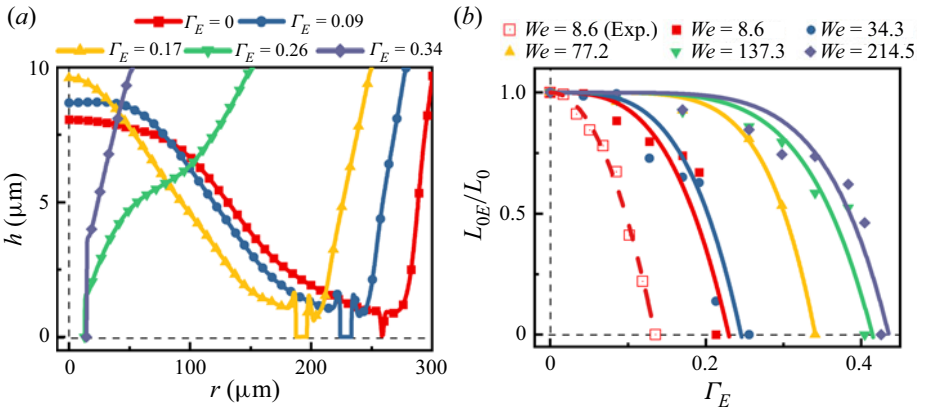


Figure 11. (*a*) The contour of the drop bottom surface at the moment of the contact with $We = 8.6$ ($Ca_g = 1.23 \times 10^{-4}$) in different external electric field intensities. (*b*) The dimensionless initial contact radius when varying the electric field strength with different impact velocities. The trend curves are obtained by fitting the data points.

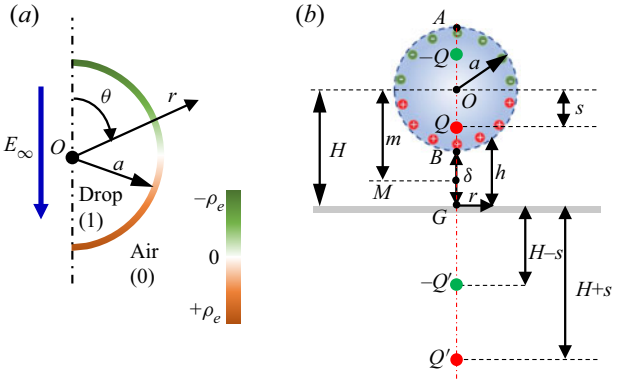


Figure 12. (*a*) Schematic representation of ρ_e distribution in polar coordinates. (*b*) Schematic diagram of the mirror charge model when the drop is close to the grounded substrate, which is simplified by the charge dipole.

Based on Gauss's theorem ($\rho_e = -\varepsilon \boldsymbol{E}_r$), the amount of electric polarization charge can be obtained by integrating the ρ_e on the top or bottom hemispherical surface,

$$Q = 2\pi \int_0^{\pi/2} \rho_e r^2 \sin(\theta)\, \mathrm{d}\theta = -3\pi\varepsilon_0 a^2 \boldsymbol{E}_\infty, \tag{4.3}$$

where the negative sign ('−') means that the electrical properties of the polarized charge (Q) is opposite to $\boldsymbol{E}_\infty$. The polarized charge obtained numerically ($Q_{Simulation}$) shows good agreement with that by theory (see supplementary figure S7), qualitatively supporting the notion that the surface polarized charge of the drop is unchanged when the drop approaches the substrate.

The separation of polarized surface charge allows us to treat the drop as a charge dipole. We further use the mirror charge model of this dipole to qualitatively explain the rapid growth of the $\boldsymbol{E}_B$ and $\boldsymbol{f}_{esB}$ at the bottom of the drop. As shown in figure 12(*b*), we assume the following. (i) The drop is approximated as a sphere that could quantify the surface charge using Taylor's solution. We note that for $\Gamma_E < 0.43$, the deformation of the drop is

https://doi.org/10.1017/jfm.2022.439 Published online by Cambridge University Press

small (with $D < 0.11$) (see figure 7), and the spherical assumption is reasonable. (ii) The charge polarization is a much more rapid process than the drop deformation ($t_E \ll t_\mu$), therefore the charge separation has completed before the deformation. (iii) The charge is distributed equally on the top and bottom of the drop hemisphere. (iv) The internal electric field of the drop is negligible. (v) The substrate is a conductive plane of zero potential. The electric field of the non-uniformly distributed induced charges can be equivalent to that generated by point charges located on the central axis of the drop. We assume the distance from the centre of the drop (point O) to the point charge is s. Here H is the distance between O and the substrate (point G). According to the method of mirror charge (Papadopoulos 1963), there is a point charge with opposite charges at a symmetrical position on the lower side of the grounded conductive substrate. The space electric field formed by the surface charge can be replaced by four equivalent point charges. First, the potential at point A on the upper of the drop is

$$\Phi_A = \frac{1}{4\pi\varepsilon_0}\left(\frac{-Q}{a-s} + \frac{Q}{a+s} + \frac{-Q'}{2H+a-s} + \frac{Q'}{2H+a+s}\right). \tag{4.4}$$

The electric potential at point B at the lower part of the drop is

$$\Phi_B = \frac{1}{4\pi\varepsilon_0}\left(\frac{-Q}{a+s} + \frac{Q}{a-s} + \frac{-Q'}{2H-a-s} + \frac{Q'}{2H-a+s}\right). \tag{4.5}$$

Because the electric field inside the drop is approximately 0,

$$\Phi_A = \Phi_B. \tag{4.6}$$

The distance between the drop and the substrate is $\delta = H - a$. Substituting that into (4.4), (4.5) and (4.6), the location of charge centre (s) is

$$s = \sqrt{-a^2 - 2a\delta - 2aH + 4H^2}. \tag{4.7}$$

Equation (4.7) suggests that s approaches a with the decrease of δ, and the charge on the surface of the drop is concentrated at point B when the drop contacts the substrate. The electric field at point B is

$$\boldsymbol{E}_B = \frac{Q}{4\pi\varepsilon_0}\left(\frac{1}{(a+s)^2} - \frac{1}{(a-s)^2} - \frac{1}{(2H-a-s)^2} + \frac{1}{(2H-a+s)^2}\right), \tag{4.8}$$

which can be simplified by substituting (4.7) into the above equation:

$$\boldsymbol{E}_B = \frac{Q}{4\pi\varepsilon_0}\left(\frac{-1}{a\delta}\right) = \frac{3a}{4\delta}E_\infty. \tag{4.9}$$

Equation (4.9) suggests that the $\boldsymbol{E}_B$ at the bottom of the drop increases sharply as δ decreases. The characteristic electric field stress $\boldsymbol{f}_{esB}$ is

$$\boldsymbol{f}_{esB} = \frac{1}{2}\varepsilon_0 \boldsymbol{E}_B{}^2 = \frac{9\varepsilon_0 a^2}{32\delta^2}\boldsymbol{E}_\infty^2. \tag{4.10}$$

Therefore, the scaling law of $\boldsymbol{E}_B$ and $\boldsymbol{f}_{esB}$ versus δ can be obtained,

$$\boldsymbol{E}_B \sim \frac{a}{\delta}\boldsymbol{E}_\infty, \quad \boldsymbol{f}_{esB} \sim \frac{\varepsilon_0 a^2}{\delta^2}\boldsymbol{E}_\infty^2. \tag{4.11a,b}$$

The (4.11a,b) can describe the rapid growth of the $\boldsymbol{E}_B$ and $\boldsymbol{f}_{esB}$ when the external electric field is within a suitable range, which is verified by the numerical simulation

https://doi.org/10.1017/jfm.2022.439 Published online by Cambridge University Press

results (see supplementary figure S6). When $\Gamma_E < 0.26$, the drop is concave; when $\Gamma_E < 0.68$, the drop undergoes significant ellipsoidal deformation. The assumption (i) in both cases is no longer precise, resulting in a noticeable deviation from the scaling law (4.11*a*,*b*).

4.2. *Scaling law for critical electric field to introduce conical tip formation*

Klaseboer, Manica & Chan (2014) showed that for the charge neutral drop impact, the profile of the drop bottom surface is governed by the balance between drop inertia and lubrication pressure. While exposed in an electric field, the additional electric stress may become comparable to the lubrication pressure. The air film is mainly affected by the combined effects of gravity, Laplace pressure ($p_\gamma = 2\gamma/a$), the lubrication pressure (p_g) and the electric stress ($\boldsymbol{f}_{esB}$). Here the gravity and surface tension are relatively small and can be neglected.

The airflow is assumed to be incompressible because p_g is much smaller than the ambient pressure ($P_0 = 10^5$ Pa) in this study, which is also confirmed by the compressibility factor $\epsilon \equiv P_0/(a\mu_0^{-1}\boldsymbol{U}^7\rho_1^4)^{1/3}$ criteria. For $\epsilon^{-1} < 3$, no significant compression of the air disc is expected (Mandre *et al.* 2009; Li & Thoroddsen 2015). In this work, ϵ^{-1} is in the range of 0.08–2 for the drop velocity (0.5–2 m s^{-1}), which suggests the incompressible flow assumption is still valid. The lubrication pressure field at the bottom of the drop can be obtained by the lubrication approximation of the Reynolds equation in an axisymmetric form (Chan, Klaseboer & Manica 2011),

$$\frac{1}{r}\frac{\partial}{\partial r}\left(\frac{h^3}{12\mu_0}r\frac{\partial p}{\partial r}\right) = \frac{\partial\,(h)}{\partial t}, \tag{4.12}$$

where h is a function of r: $h = \delta + a - \sqrt{a^2 - r^2}$. Integrating both sides and rewriting the equation, we obtain

$$p_g(r) = -3\mu_0\frac{\delta + a - 2\sqrt{a^2 - r^2}}{(\delta + a - (a^2 - r^2))^2}\frac{\partial H}{\partial t} - 3\mu_0\frac{1}{a}\boldsymbol{U}. \tag{4.13}$$

Recognizing the air viscosity is relatively small at the position of the drop axis (when $r = 0$), p_g can be simplified as

$$p_g = \frac{3\mu_0 a}{\delta^2}\boldsymbol{U}. \tag{4.14}$$

The scaling law of the Γ_E, the critical value that is sufficient to induce the formation of the conical tip, is obtained by comparing $\boldsymbol{f}_{esB}$ and p_g of the drop:

$$\boldsymbol{f}_{esB} \sim p_g \Rightarrow \boldsymbol{E}_\infty^2 \sim \frac{\mu_0\boldsymbol{U}}{\varepsilon_0 a} \Rightarrow \Gamma_E \propto \sqrt{Ca_g}. \tag{4.15}$$

The numerical and experimental data for different Γ_E and Ca_g are plotted in figure 13, together with the critical dimensionless strength of electric field (solid line) predicted by fitting equation (4.15). Both the numerical and experimental data are in good agreement with (4.15), which shows a positive correlation between Γ_E and Ca_g. Even with relatively high Ca_g, the electric field is well below the Taylor limit of critical field, which is not a harsh requirement to achieve the goal of regulating the impact dynamics and avoiding the air entrapment.

https://doi.org/10.1017/jfm.2022.439 Published online by Cambridge University Press

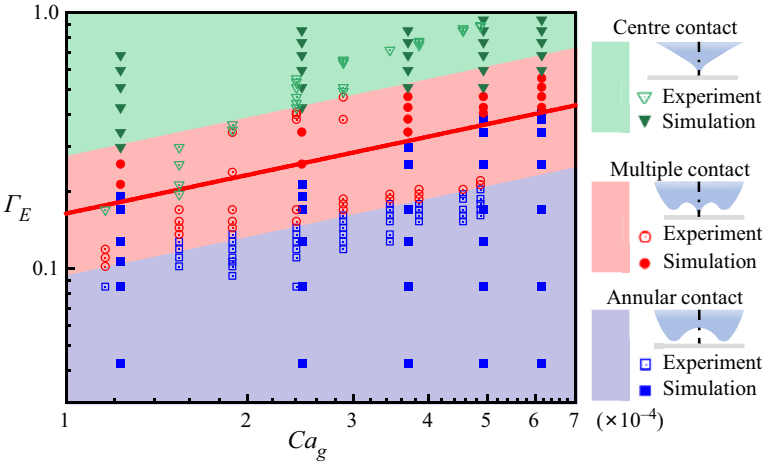


Figure 13. Experimental data and simulation data versus the critical dimensionless electric field strength. The solid curves are the critical dimensionless electric field strength predicted by (4.15).

5. Conclusions

The EHD behaviour of air entrapment when a neutral drop impacts onto a flat solid surface under an external electric field is investigated experimentally and numerically. The electric field may entirely change the behaviour of air entrapment by altering the initial contact state during the drop impact on a flat smooth surface. The electric field introduces the polarized charge that is concentrated at the bottom poles of the drop. Notably, the electric stress at the bottom of the drop ($\boldsymbol{f}_{esB}$) increases rapidly due to the locally intensified charge density at the surface when the distance between the drop and the substrate is within one millimetre. In this very short time and small space, $\boldsymbol{f}_{esB}$ dominates the subsequent air entrapment and the contact state of the drop with the substrate. Three representative contact modes (annular contact mode, multiple contact mode and centre contact mode) and subsequent air film evolution processes with different level of dimensionless electric field (Γ_E) are studied. Two key factors that determine the contact mode can be obtained: the bottom shape of the drop and the instantaneous velocity $\boldsymbol{U}_B$, both of which depend on the Γ_E.

As the Γ_E is raised above a critical value, the electric stress counteracts the effect of the lubrication pressure and forms a conical tip at the bottom of the drop quickly instead of a dimple. The centre contact of the tip on the substrate generates a circular contact line moving outwards with the air film still connecting to the external atmosphere, resulting in no air bubble trapped. The critical Γ_E only depends on the square root of capillary number based on the air viscosity ($\Gamma_E \propto \sqrt{Ca_g}$), which is built based on the dipole mirror charge model. This scaling law of the critical electric field is verified experimentally and numerically. This work brings insights for mitigating bubbles and voids defects into applications such as inkjet printing and droplet-based additive manufacturing.

Supplementary material and movies. Supplementary material and movies are available at https://doi.org/10.1017/jfm.2022.439.

Funding. This work was supported by the National Key Research and Development Program of China (no. 2021YFB3200700), the National Natural Science Foundation of China (grant nos. 11932009 and 51906073), the Natural Science Foundation of HuBei Province (2020CFA028) and the Academic Frontier

https://doi.org/10.1017/jfm.2022.439 Published online by Cambridge University Press

Youth Team of Huazhong University of Science and Technology (2017QYTD05). The computation is completed in the HPC Platform of Huazhong University of Science and Technology.

Declaration of interests. The authors report no conflict of interest.

Author ORCIDs.
Yu Tian https://orcid.org/0000-0002-1646-3742;
Yanchu Liu https://orcid.org/0000-0003-4091-7625;
Zihan Peng https://orcid.org/0000-0003-2925-0188;
Chenghao Xu https://orcid.org/0000-0001-5681-0553;
Dong Ye https://orcid.org/0000-0001-5956-8862;
Yin Guan https://orcid.org/0000-0003-0478-0094;
Xinping Zhou https://orcid.org/0000-0001-6340-5273;
Weiwei Deng https://orcid.org/0000-0002-8331-9249;
YongAn Huang https://orcid.org/0000-0001-7713-8380.

Author contributions. Y. Tian and Y. Liu contributed equally to this work.

References

Antonini, C., Lee, J.B., Maitra, T., Irvine, S., Derome, D., Tiwari, M.K., Carmeliet, J. & Poulikakos, D. 2014 Unraveling wetting transition through surface textures with x-rays: liquid meniscus penetration phenomena. *Sci. Rep.* **4** (1), 4055.

Basaran, O.A. & Scriven, L.E. 1989 Axisymmetric shapes and stability of charged drops in an external electric-field. *Phys. Fluids* A **1** (5), 799–809.

Bouwhuis, W., van der Veen, R.C.A., Tuan, T., Keij, D.L., Winkels, K.G., Peters, I.R., van der Meer, D., Sun, C., Snoeijer, J.H. & Lohse, D. 2012 Maximal air bubble entrainment at liquid-drop impact. *Phys. Rev. Lett.* **109** (26), 264501.

Chan, D.Y.C., Klaseboer, E. & Manica, R. 2011 Film drainage and coalescence between deformable drops and bubbles. *Soft Matt.* **7** (6), 2235–2264.

Collins, R.T., Sambath, K., Harris, M.T. & Basaran, O.A. 2013 Universal scaling laws for the disintegration of electrified drops. *Proc. Natl Acad. Sci. USA* **110** (13), 4905–4910.

van Dam, D.B. & Clerc, C.L. 2004 Experimental study of the impact of an ink-jet printed droplet on a solid substrate. *Phys. Fluids* **16** (9), 3403–3414.

Derby, B. 2010 Inkjet printing of functional and structural materials: fluid property requirements, feature stability, and resolution. *Annu. Rev. Mater. Res.* **40**, 395–414.

Gao, F., Yi, H., Qi, L., Qiao, R. & Deng, W. 2019 Weakly charged droplets fundamentally change impact dynamics on flat surfaces. *Soft Matt.* **15** (28), 5548–5553.

García-Geijo, P., Riboux, G. & Gordillo, J.M. 2020 Inclined impact of drops. *J. Fluid Mech.* **897**, A12.

Gawande, N., Mayya, Y.S. & Thaokar, R. 2020 Jet and progeny formation in the rayleigh breakup of a charged viscous drop. *J. Fluid Mech.* **884**, A31.

Grimm, R.L. & Beauchamp, J.L. 2005 Dynamics of field-induced droplet ionization: time-resolved studies of distortion, jetting, and progeny formation from charged and neutral methanol droplets exposed to strong electric fields. *J. Phys. Chem.* B **109** (16), 8244–8250.

Ha, J.W. & Yang, S.M. 2000 Deformation and breakup of newtonian and non-newtonian conducting drops in an electric field. *J. Fluid Mech.* **405**, 131–156.

Herrada, M.A., Lopez-Herrera, J.M., Ganan-Calvo, A.M., Vega, E.J., Montanero, J.M. & Popinet, S. 2012 Numerical simulation of electrospray in the cone-jet mode. *Phys. Rev.* E **86** (2 Pt 2), 026305.

Hicks, P.D., Ermanyuk, E.V., Gavrilov, N.V. & Purvis, R. 2012 Air trapping at impact of a rigid sphere onto a liquid. *J. Fluid Mech.* **695**, 310–320.

Hicks, P.D. & Purvis, R. 2010 Air cushioning and bubble entrapment in three-dimensional droplet impacts. *J. Fluid Mech.* **649**, 135–163.

Huang, Y., Wu, H., Xiao, L., Duan, Y., Zhu, H., Bian, J., Ye, D. & Yin, Z. 2019 Assembly and applications of 3d conformal electronics on curvilinear surfaces. *Mater. Horizons* **6** (4), 642–683.

https://doi.org/10.1017/jfm.2022.439 Published online by Cambridge University Press

JIAN, Z., CHANNA, M.A., KHERBECHE, A., CHIZARI, H., THORODDSEN, S.T. & THORAVAL, M.J. 2020 To split or not to split: dynamics of an air disk formed under a drop impacting on a pool. *Phys. Rev. Lett.* **124** (18), 184501.

JOSSERAND, C. & THORODDSEN, S.T. 2016 Drop impact on a solid surface. *Annu. Rev. Fluid Mech.* **48** (1), 365–391.

KLASEBOER, E., MANICA, R. & CHAN, D.Y. 2014 Universal behavior of the initial stage of drop impact. *Phys. Rev. Lett.* **113** (19), 194501.

KUMAR, R., SHUKLA, R.K., KUMAR, A. & KUMAR, A. 2020 A computational study on air entrapment and its effect on convective heat transfer during droplet impact on a substrate. *Intl J. Therm. Sci.* **153**, 106363.

LANGLEY, K.R., CASTREJON-PITA, A.A. & THORODDSEN, S.T. 2020 Droplet impacts onto soft solids entrap more air. *Soft Matt.* **16** (24), 5702–5710.

LEE, J.S., WEON, B.M., JE, J.H. & FEZZAA, K. 2012 How does an air film evolve into a bubble during drop impact? *Phys. Rev. Lett.* **109** (20), 204501.

LI, E.Q., LANGLEY, K.R., TIAN, Y.S., HICKS, P.D. & THORODDSEN, S.T. 2017*b* Double contact during drop impact on a solid under reduced air pressure. *Phys. Rev. Lett.* **119** (21), 214502.

LI, E.Q. & THORODDSEN, S.T. 2015 Time-resolved imaging of a compressible air disc under a drop impacting on a solid surface. *J. Fluid Mech.* **780**, 636–648.

LI, E.Q., VAKARELSKI, I.U. & THORODDSEN, S.T. 2015 Probing the nanoscale: the first contact of an impacting drop. *J. Fluid Mech.* **785**, R2.

LI, D., ZHANG, D., ZHENG, Z. & TIAN, X. 2017*a* Numerical analysis on air entrapment during a droplet impacts on a dry flat surface. *Intl J. Heat Mass Transfer* **115**, 186–193.

LIGON, S.C., LISKA, R., STAMPFL, J., GURR, M. & MULHAUPT, R. 2017 Polymers for 3d printing and customized additive manufacturing. *Chem. Rev.* **117** (15), 10212–10290.

LIU, Y., TAN, P. & XU, L. 2013 Compressible air entrapment in high-speed drop impacts on solid surfaces. *J. Fluid Mech.* **716**, R9.

LIU, Y., TAN, P. & XU, L. 2015 Kelvin–Helmholtz instability in an ultrathin air film causes drop splashing on smooth surfaces. *Proc. Natl Acad. Sci. USA* **112** (11), 3280–3284.

MANDRE, S., MANI, M. & BRENNER, M.P. 2009 Precursors to splashing of liquid droplets on a solid surface. *Phys. Rev. Lett.* **102** (13), 134502.

MEHDI-NEJAD, V., MOSTAGHIMI, J. & CHANDRA, S. 2003 Air bubble entrapment under an impacting droplet. *Phys. Fluids* **15** (1), 173–183.

MINEMAWARI, H., YAMADA, T., MATSUI, H., TSUTSUMI, J., HAAS, S., CHIBA, R., KUMAI, R. & HASEGAWA, T. 2011 Inkjet printing of single-crystal films. *Nature* **475** (7356), 364–367.

ORATIS, A.T., BUSH, J.W.M., STONE, H.A. & BIRD, J.C. 2020 A new wrinkle on liquid sheets: turning the mechanism of viscous bubble collapse upside down. *Science* **369** (6504), 685–688.

PAPADOPOULOS, M. 1963 Classical electrodynamics (JD Jackson). *SIAM Rev.* **5** (1), 82.

ROGHAIR, I., MUSTERD, M., VAN DEN ENDE, D., KLEIJN, C., KREUTZER, M. & MUGELE, F. 2015 A numerical technique to simulate display pixels based on electrowetting. *Microfluid. Nanofluid.* **19** (2), 465–482.

SANTRA, S., MANDAL, S. & CHAKRABORTY, S. 2018 Electrohydrodynamics of confined two-dimensional liquid droplets in uniform electric field. *Phys. Fluids* **30** (6), 062003.

SAVILLE, D.A. 1997 Electrohydrodynamics: the Taylor–Melcher leaky dielectric model. *Annu. Rev. Fluid Mech.* **29**, 27–64.

SENGUPTA, R., WALKER, L.M. & KHAIR, A.S. 2017 The role of surface charge convection in the electrohydrodynamics and breakup of prolate drops. *J. Fluid Mech.* **833**, 29–53.

SHEN, D., ZOU, G., LIU, L., DULEY, W.W. & ZHOU, Y.N. 2016 Investigation of splashing phenomena during the impact of molten sub-micron gold droplets on solid surfaces. *Soft Matt.* **12** (1), 295–301.

SHUKLA, R.K., KUMAR, A., KUMAR, R., SINGH, D. & KUMAR, A. 2019 Numerical study of pore formation in thermal spray coating process by investigating dynamics of air entrapment. *Surf. Coat. Technol.* **378**, 124972.

SINGH, M., HAVERINEN, H.M., DHAGAT, P. & JABBOUR, G.E. 2010 Inkjet printing-process and its applications. *Adv. Mater.* **22** (6), 673–685.

SNOEIJER, J.H. & ANDREOTTI, B. 2013 Moving contact lines: scales, regimes, and dynamical transitions. *Annu. Rev. Fluid Mech.* **45** (1), 269–292.

STRINGER, J., *et al.* 2016 Integration of additive manufacturing and inkjet printed electronics: a potential route to parts with embedded multifunctionality. *Manuf. Rev.* **3** (12), 2265–4224.

TAYLOR, G.I. 1966 Studies in electrohydrodynamics. I. The circulation produced in a drop by electrical field. *Proc. Math. Phys. Engng Sci.* **291** (1425), 159–166.

https://doi.org/10.1017/jfm.2022.439 Published online by Cambridge University Press

THORAVAL, M.J., TAKEHARA, K., ETOH, T.G. & THORODDSEN, S.T. 2013 Drop impact entrapment of bubble rings. *J. Fluid Mech.* **724**, 234–258.

THORODDSEN, S.T., ETOH, T.G. & TAKEHARA, K. 2003 Air entrapment under an impacting drop. *J. Fluid Mech.* **478**, 125–134.

THORODDSEN, S.T., ETOH, T.G. & TAKEHARA, K. 2008 High-speed imaging of drops and bubbles. *Annu. Rev. Fluid Mech.* **40** (1), 257–285.

THORODDSEN, S.T., ETOH, T.G., TAKEHARA, K., OOTSUKA, N. & HATSUKI, Y. 2005 The air bubble entrapped under a drop impacting on a solid surface. *J. Fluid Mech.* **545** (-1), 203–212.

VAN DER VEEN, R.C.A., TUAN, T., LOHSE, D. & SUN, C. 2012 Direct measurements of air layer profiles under impacting droplets using high-speed color interferometry. *Phys. Rev.* E **85** (2), 026315.

VLAHOVSKA, P.M. 2019 Electrohydrodynamics of drops and vesicles. *Annu. Rev. Fluid Mech.* **51** (1), 305–330.

VO, Q. & TRAN, T. 2021 Mediation of lubricated air films using spatially periodic dielectrophoretic effect. *Nat. Commun.* **12** (1), 4289.

WAGONER, B.W., VLAHOVSKA, P.M., HARRIS, M.T. & BASARAN, O.A. 2020 Electric-field-induced transitions from spherical to discocyte and lens-shaped drops. *J. Fluid Mech.* **904**, R4.

WANG, Z., TIAN, Y., ZHANG, C., WANG, Y. & DENG, W. 2021 Massively multiplexed electrohydrodynamic tip streaming from a thin disc. *Phys. Rev. Lett.* **126** (6), 064502.

WU, H., TIAN, Y., LUO, H., ZHU, H., DUAN, Y. & HUANG, Y. 2020 Fabrication techniques for curved electronics on arbitrary surfaces. *Adv. Mater. Technol.* **5** (8), 2000093.

XIONG, W. & CHENG, P. 2018 Numerical investigation of air entrapment in a molten droplet impacting and solidifying on a cold smooth substrate by 3d lattice Boltzmann method. *Intl J. Heat Mass Transfer* **124**, 1262–1274.

YANG, W., DUAN, H., LI, C. & DENG, W. 2014 Crossover of varicose and whipping instabilities in electrified microjets. *Phys. Rev. Lett.* **112** (5), 054501.

YARIN, A.L. 2006 Drop impact dynamics: splashing, spreading, receding, bouncing. *Annu. Rev. Fluid Mech.* **38**, 159–192.

YI, H.H., QI, L., LUO, J., JIANG, Y. & DENG, W. 2016 Pinhole formation from liquid metal microdroplets impact on solid surfaces. *Appl. Phys. Lett.* **108** (4), 041601.

ZHANG, J., ZAHN, J.D. & LIN, H. 2013 Transient solution for droplet deformation under electric fields. *Phys. Rev.* E **87** (4), 043008.

https://doi.org/10.1017/jfm.2022.439 Published online by Cambridge University Press